Radial-flow cell exploiting the activation of commercial carbon felt to improve capacitive deionization for water softening

Radial-flow cell using commercial activated carbon felt as a strategy to improve capacitive deionization for water softening

Bruno G. M. Alves[1], Davide Arcoraci[2], Alessandro Pedico[2,3], Andrea Lamberti[2], Luís A. M. Ruotolo[1*]

[1]*Department of Chemical Engineering, Federal University of São Carlos, Rodovia Washington Luiz, km 235, São Carlos, SP, 13565-905, Brazil*
[2]*Dipartimento di Scienza Applicata e Tecnologia (DISAT), Politecnico di Torino, Corso Duca degli Abruzzi 24, Torino 10129, Italy*
[3]*Istituto Nazionale di Ricerca Metrologica (INRiM), Strada delle Cacce 91, Torino 10135, Italy*

[*]Corresponding author: pluis@ufscar.br

Abstract

Exponential growth of interest in capacitive deionization (CDI) technology has been motivated by its low energy consumption and potential use in desalination and water softening. In this work, CDI was applied for water softening using a radial-flow cell designed according to the concept of a "percolation flow cell", combining flow-through and flow-by configurations to achieve high efficiencies and electrosorption rates. To make this cell economically viable, the electrode was a commercial activated carbon felt (CF) with high specific surface area. The felt was chemically modified to create surface functional groups that could minimize the co-ion repulsion effect, while the use of asymmetric electrodes improved the electrosorption capacity. Considering the variation of mass transfer and residence time along the radial flow, two flow patterns were studied: (*i*) from the center of the electrode to the edge (CE), and (*ii*) from the edge to the center of the electrode (EC). For each configuration, evaluation was made of the effects of the applied current and flow rate, enabling determination of the influence of charge and mass transfer processes on the charging efficiency and the ion removal rate. The results indicated that modification of the CF using nitric acid to introduce negative oxygen groups on the surface was highly effective, with a 44.3% improvement in capacitance, while the use of ethylenediamine led to only modest enhancement. The radial-flow cell showed a significant dependence on the flow direction. The EC flow provided a more uniform ionic flux convergence, which improved charge efficiency and ion transport, with optimal operation achieved at 1.25 A m^{-2} and 22 mL min^{-1}. Under these conditions, combined with the EC flow direction, the system presented a salt adsorption capacity (SAC) of 25.04 mg g^{-1} and specific energy consumption of 0.50 J mg^{-1}. The balance between performance and energy efficiency demonstrated the potential of this system for use in practical water treatment applications.

1. Introduction

Water is considered "hard" when it has high concentrations of certain ions, especially calcium and magnesium. Water hardness is measured in mg L^{-1} of $CaCO_3$, according to which water can be classified as being moderately hard (135-200 mg L^{-1}), hard (200-350 mg L^{-1}), or very hard (above 350 mg L^{-1}) [1]. Although hard water is not a problem in most everyday applications, a well-known drawback of this type of water is its capacity to precipitate soap, inhibiting the formation of foam. Concerning potability, Brazilian legislation stipulates a maximum total concentration of 500 mg L^{-1} of calcium and magnesium, since higher values affect the organoleptic properties of water, giving it an unpleasant metallic taste. In industrial processes, hard water can result in the formation of deposits of insoluble calcium and magnesium compounds in equipment such as boiler pipes and heat exchangers, reducing heat exchange efficiency and increasing the risk of accidents. Furthermore, it is often necessary to reduce the hardness of water in residences, affecting the daily lives of millions of people [2]. Therefore, it is increasingly desirable to encourage the development of technologies capable of removing ions from aqueous media, with the aim of softening water.

The main technologies currently available for water softening include ion exchange (IE), reverse osmosis (RO), and electrodialysis (EDI). IE uses polymeric resins that require chemical products for their regeneration, while high energy consumption in RO and EDI is associated with the need for high pressures (RO, 1.0 kWh m^{-3}) and voltages (EDI, 2.03 kWh m^{-3}), in addition to the use of membranes that increase the capital cost and also suffer from fouling [3,4].

As an alternative, capacitive deionization (CDI) has emerged as an attractive technique for water softening, using the principles of electrical double layer capacitance for the electrosorption of cations and anions [5]. Its advantages include use at low pressures [6], no requirement for membranes or added chemicals, and ease of operation and maintenance (Fig. S1). For large-scale applications, since this is a system that works as a capacitor, there is also the possibility of recovering part of the energy stored during the electrosorption cycle [7,8]. From an energy perspective, the application of CDI can be competitive, considering the ion concentrations involved in water softening processes. It has been reported that for concentrations lower than 5,000 mg L^{-1}, the use of CDI technology in a desalination process could have lower energy consumption than RO (1.0 kWh m^{-3}), considering an efficiency of 70% [3]. These positive aspects have resulted in exponential growth in the number of studies concerning CDI over the last 10 years (Fig. S2a). However, as shown in Fig. S2b, the number of investigations related to the use of CDI for water softening remains relatively low.

As a contribution to the advancement of capacitive deionization, this work reports the development of an electrochemical cell with the electrodes arranged so that the electrolyte flow was radial, combining flow-through and flow-by modes, in a configuration known as “percolation flow cell” (PFC) [9]. In the radial configuration, the residence time and the mass transfer rate vary in the flow direction. Therefore, investigation was made of the flow direction, from the center of the electrode to the edge, and vice versa. The operational conditions of current density and flow rate were also evaluated, to minimize the specific energy consumption (kWh per m^3 of softened water).

To obtain a practically viable system, commercially available activated carbon felt electrodes were used. In another complementary approach, the surfaces of these electrodes were modified by the introduction of oxygen and nitrogen functional groups, creating surface charges enabling use of the electrodes in an asymmetric configuration to enhance ion storage and charge efficiency [10,11]. This modification can minimize the negative influence of co-ion repulsion, leading to faster ion removal by the equipment [12].

Hypotheses adopted for development of the percolation cell with radial flow

Several CDI architectures and configurations have been reported in the literature [13,14], many of which are impractical from operational or scale-up perspectives, while little attention has been paid to the influence of the electrode regeneration time on productivity (volume of deionized water per volume of water fed). Hence, there is a gap in knowledge concerning the effect of the cell architecture in relation to the desorption cycle. Therefore, the present study conceived the use of a cell with radial flow, since this flow pattern would enable a 50% reduction of the electrolyte residence time within the electrode during the desorption cycle, consequently increasing productivity. Considering the electrosorption step, the following hypotheses were adopted in the design of the proposed CDI cell: (*i*) the use of a carbon felt electrode would facilitate charge transfer by reducing the solid phase resistance and the ohmic drop; (*ii*) the use of the PFC (percolation flow cell) configuration would have the advantages of the flow-by configuration, in terms of electric field distribution and residence time, combined with the advantage of the flow-through configuration [15] of increasing the coefficient of mass transfer external to the fiber (*k*m), as shown in Fig. 1a, where k_m is the ratio between the diffusion coefficient of the chemical species (D_{iff}) and the thickness of the diffusive boundary layer (δ); (*iii*) the radial flow with flow from the center to the edges of the electrode (Fig. 1b), represented by $\vec{u}$, where *u* is the flow velocity, would lead to a decrease in *k*m, due to the increase of δ along the radial position, as a function of the decrease in flow velocity (Fig. 1c: $u_1 > u_2 > u_3$, since A_{s2} increases). On the other hand, there are increases of the residence time ($\tau_3 > \tau_2 > \tau_1$) and the area available for adsorption, which act to favor electrosorption; (*iv*) the radial flow with flow from the edges to the center of the electrode (Fig. 1b), represented by $\overleftarrow{u}$, would have an effect opposite to that described in hypothesis (*iii*).

Hypotheses (*i*) and (*ii*) were validated in previous work by the same research group [16,17]. However, the influence of flow direction on capacitive deionization performance has not previously been explored, with hypotheses (*iii*) and (*iv*) still requiring more detailed investigation, especially considering the notable difference in the concentration gradients (∇C) for the two flow patterns, which could strongly influence the mass transfer external to the fiber and, therefore, the kinetics of the electrosorption process.

Given the above considerations, a radial-flow cell was designed and built to study the effects of fluid dynamic and operational variables on deionization performance.

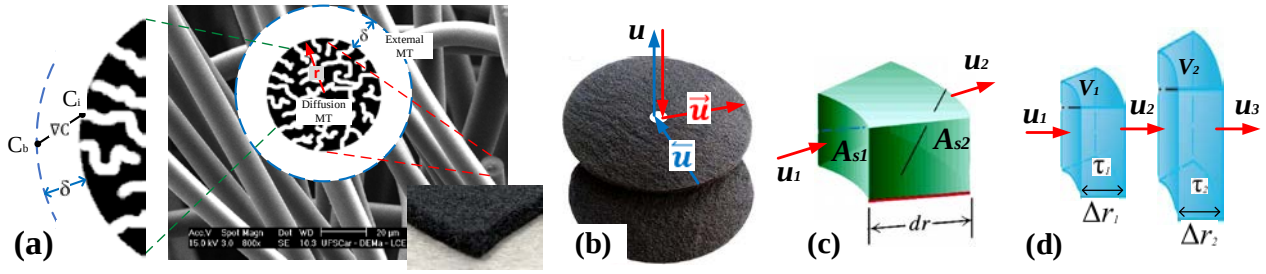

Fig. 1. (a) Schematic representation of the mass transfer (MT) processes within and outside the carbon felt fiber, where C_b and C_i are the bulk and interfacial concentrations, respectively; (b) circular electrode with representation of the flows from the center to the edge (in red) and from the edge to the center (in blue); (c) variation of the radial flow velocity, as a function of the increase in the cross-sectional area (A_{st}); (d) representation of the variation of the electrode volume (V), as a function of the radius, and its effect on the residence time ($\tau = V/\dot{V}$, where $\dot{V}$ is the electrolyte flow rate).

2. Experimental

2.1. Electrode material and surface modification

Commercial carbon felt (CF) (type ACN-211-20, fabricated by the Germany company Kynol®) was used in this work. To create asymmetry between the electrodes, experiments were performed to modify the CF surface by inserting functional groups. Negatively charged functional groups were added using concentrated and diluted HNO_3, according to the conditions shown in Table S1. Conversely, positively charged groups were added using ethylenediamine ($C_2H_8N_2$ or EDA), after a pretreatment with HNO_3, as suggested elsewhere [18]. Only the HNO_3-pretreated sample that presented the best electrochemical performance was subsequently modified with EDA.

The electrodes were evaluated and compared by electrochemical characterizations performed using a Swagelok® three-electrode cell with a 6 mm diameter modified CF as the working electrode (WE), two pieces of pristine CF (12 mm) as the counter electrode (CE), a cellulose filter as a separator, and an Ag/AgCl reference electrode (Fig. S3). The techniques used were cyclic voltammetry (CV), galvanostatic charge and discharge (GCD), and electrochemical impedance spectrometry (EIS). EIS was used to acquire resistance and capacitance data, including the charge-transfer resistance (R_{CT}) and the capacitance of the electrical double layer (C_{EIS}). The capacitance obtained by EIS was used to determine the potential of zero charge (E_{pzc}) [17]. Aqueous 0.5 M K_2SO_4 was used in the CV, GCD, and EIS analyses, while 1000 mg L^{-1} K_2SO_4 was used in the EIS measurements to determine E_{pzc}.

The specific capacitances obtained using cyclic voltammetry (C_{CV}), EIS (C_{EIS}), and GCD (C_{GCD}), in F per gram of CF, were calculated using Eqs. 1-3, respectively. In these equations, I is the current, v is the scan rate, m is the mass of CF, E is the electrode potential, ω is the angular frequency, Z'' is the imaginary component of the Nyquist plot, I_d is the discharging current, t_d is the discharging time, and ΔE is the cut-off potential. It should be noted that the lowest EIS frequency (10 mHz) was used to calculate C_{EIS}. Additionally, the GCD data were used to determine the coulombic (ε_C) and energy (ε_E) efficiencies, using Eqs. 4 and 5, respectively, where Q_d is the charge delivered during the discharge, Q_c is the charge stored during the electrode charging, and E_{we} is the working electrode potential [19].

$$C_{CV} = \frac{\int_{E_1}^{E_2} I \, dE}{\int_0^{ch} \nu m (E_1 - E_2)} \quad (1)$$

$$C_{EIS} = \frac{1}{|\omega Z''|} \quad (2)$$

$$C_{GCD} = \frac{I_d \, t_d}{m \Delta E} \quad (3)$$

$$\varepsilon_C = \frac{Q_d}{Q_c} 100\% \quad (4)$$

$$\varepsilon_E = \frac{\int_{t_{ch}}^{t_d} E_{we} \, I \, dt}{\int_0^{ch} E_{we} \, I \, dt} \, 100\% \quad (5)$$

2.2. Radial-flow CDI cell

The design of the radial-flow cell was based on preliminary experiments using a conventional axial flow reactor [9], where the cell geometry was defined as radial, with the aim of halving the residence time during the desorption cycle, which would improve the water recovery parameter (*WR*). The electrode porosity was considered as 0.78, based on previous results [16], corresponding to one felt layer (1.5 mm) as cathode and anode.

Fig. 2a shows a schematic illustration of the CDI cell with radial flow. The cell contained three electrode stacks (cathode + anode) composed of carbon felt, circular in shape (outer diameter of 240 mm), with a central hole (diameter of 4 mm) for the electrolyte flow, resulting in a solution percolation path of 100 mm (shown in Fig. 1b). The electrical contacts were stainless steel and the separators were cellulose filters. The electrode + electrical contact + separator assemblies were placed in a cylindrical polycarbonate tube, with a central hole at the top of the cell and another at its base, so that the flow could be established both from the center to the edges and in the opposite direction. Fig. S4 shows photographs of the cell.

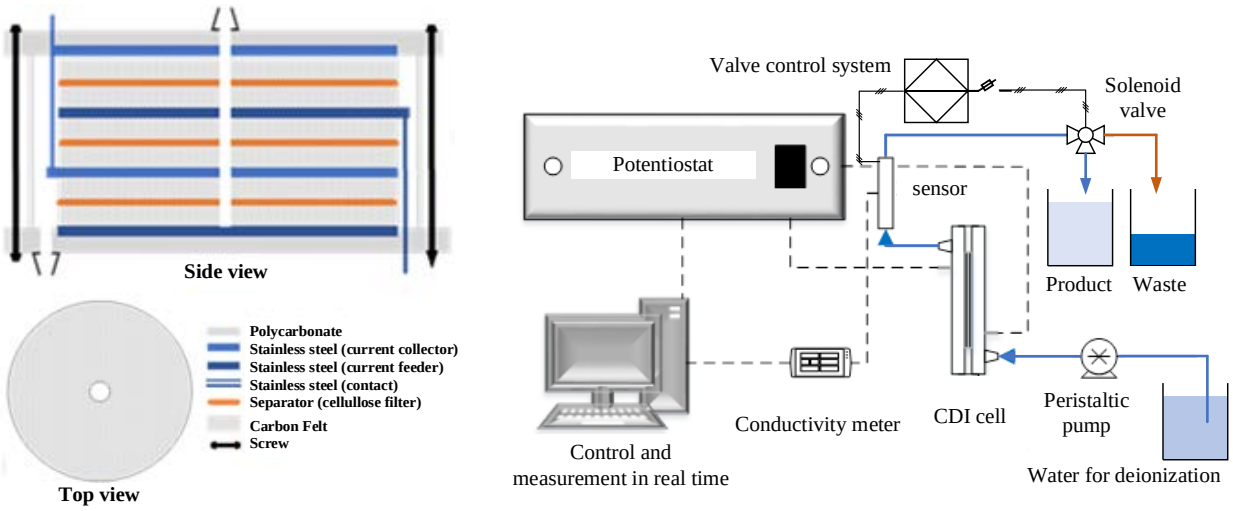

(a) (b)

Fig. 2. (a) Schematic representation of the radial-flow CDI cell and its main components. (b) Experimental system for CDI in single-pass mode, with automated control of product and waste collection.

2.3. Deionization procedure

For the study of water softening, calcium and magnesium nitrates were used as sources of Ca^{2+} and Mg^{2+} ions, with concentrations ranging from 500 to 1000 mg L^{-1}. All the solutions were prepared using ultrapure water.

To maximize productivity, while minimizing the energy cost, it was necessary to optimize the efficiency of the softening process, which was influenced by the operational mode (potentiostatic or

galvanostatic), hydrodynamic aspects, and operational parameters including flow rate and ion concentration. For the operational mode, considering that the focus of this study was on the development of a CDI cell that could realistically be employed in commercial equipment, the galvanostatic mode and continuous feeding (single-pass) were adopted (shown schematically in Fig. 2b). Selection of the galvanostatic mode was based on previous results indicating that it could provide higher charging efficiency and faster deionization [9,20]. However, it should be noted that use of the galvanostatic mode required adequate control of the cell potential (cutoff potentials), since the electrosorption/desorption cycles were limited by the maximum voltage allowed, avoiding Faradaic reactions, loss of efficiency, and degradation of the electrode [21].

The experimental procedure consisted of circulating the electrolyte through the CDI cell using a peristaltic pump. After leaving the cell, the electrolyte passed through a conductivity sensor that provided values recorded in real time. The desired electric current was applied with a potentiostat and the cell potential was recorded and displayed in real time. When the pre-established cutoff potentials were reached (1.2 V in electrosorption and 0.04 V in desorption), the polarization of the electrodes was reversed, establishing the electrosorption and desorption cycles.

To determine water recovery (*WR*), considered as the ratio between the volume of product collected and the total volume processed, the experimental system shown in Fig. 2b was modified by incorporating an automated control system for collecting deionized water and waste water. When the conductivity indicated by the conductivity sensor was below the established setpoint value, the system collected deionized water as product, by directly polarizing a three-way solenoid valve. On the other hand, when the conductivity at the cell outlet exceeded the setpoint value, the polarity of the solenoid valve was reversed, so that the flow was directed to a waste reservoir. Further details of the control system and sensor calibration are provided in Section S1 of the Supplementary Material.

The deionization experiments were performed according to the sequence shown in Table 1. Experiments 1-8 systematically evaluated the effects of the variables current density (*j*), electrolyte volumetric flow rate ($\dot{V}$), and flow direction (center-to-edge (CE) and edge-to-center (EC)) on the performance variables. The values of *j* and $\dot{V}$ were defined from previous experiments, applying values higher and lower than those shown in Table 1. Once the best operating conditions had been identified, evaluation was made of the effects of the concentration and composition of the electrolyte containing Mg^{2+} and/or Ca^{2+} cations (experiments 9-10). Finally, under the optimized conditions, experiment 11 was performed using the automated control system for collection of the product and waste, with subsequent determination of *WR*.

The performance of the deionization process was evaluated using the metrics salt adsorption capacity (*SAC*), charge efficiency (Q_E), and specific energy consumption (η). The *SAC* value (Eq. 6), indicating the amount of salt removed per unit mass of the electrode, is an essential parameter for assessing the desalination capacity of the process, which varies according to the operational conditions. In Eq. 6, $C(t)$ is the salt concentration in the electrolyte at time t, t_1 and t_2 indicate the electrosorption time interval, and m is the mass of the electrodes. Q_E (Eq. 7) indicates the percentage of the electrical charge supplied to the system that is effectively used to retain the ions in the electrode pores [16], while η (Eq. 8) indicates the energy required to remove 1 mg of salt from the electrolyte. In these equations, z is the charge of the cation, F is the Faraday constant, M is the molar mass of the salt, I is the electric current supplied in the electrosorption stage, E_{cell} is the cell potential, and m_{rem} is the mass of salt removed.

$$\boldsymbol{SAC} = \frac{\dot{\boldsymbol{V}} \int_{t_1}^{t_2} \boldsymbol{C}(\boldsymbol{t})\, \mathbf{d}\boldsymbol{t}}{\boldsymbol{m}} \tag{6}$$

$$\boldsymbol{Q_E} = \frac{\boldsymbol{zFmSAC}}{\boldsymbol{M} \int_{t_1}^{t_2} \boldsymbol{I}\, \boldsymbol{dt}} \tag{7}$$

$$\boldsymbol{\eta} = \frac{\boldsymbol{E_{cell}} \int_{t_1}^{t_2} \boldsymbol{I}\, \mathbf{d}\boldsymbol{t}}{\boldsymbol{m_{rem}}} \tag{8}$$

The water recovery (*WR*) was calculated as the ratio between the volume of water product (V_{WP}) and the total volume of water (V_T) that passed through the cell (Eq. 9).

$$\boldsymbol{WR} = \frac{\boldsymbol{V_{WP}}}{\boldsymbol{V_T}} \tag{9}$$

Table 1. Experimental conditions employed for deionization using the radial-flow CDI cell.

Experiment	j (A m^{-2})	$\dot{V}$ (mL min^{-1})	Flow direction	Cations
1	1.875	22	CE	Mg^{2+}
2	1.25	22	CE	
3	1.875	11	CE	
4	1.25	11	CE	
5	1.875	22	EC	
6	1.25	22	EC	
7	1.875	11	EC	
8	1.25	11	EC	
9	Best	Best	Best	Ca^{2+}
10	Best	Best	Best	Ca^{2+} and Mg^{2+}
11	Optimized	Optimized	Optimized	Mg^{2+}

3. Results and discussion

3.1. Electrode material

CDI is an electrochemical process in which ions are adsorbed in the electrical double layer formed at the electrode/electrolyte interface, due to the application of an electric field (Fig. S1). Therefore, the electrical properties of the interface define the capacity and effectiveness of a given material as a potential electrode for use in CDI. A suitable material should have high electrical conductivity, chemical and electrochemical stability, high specific surface area (SSA), an appropriate pore distribution, and good wettability [22,23]. Considering these aspects, carbon materials such as activated carbons, carbon nanotubes, graphene, and carbon aerogels have been highlighted for use in electrosorption processes. When the cost of the material is taken into consideration, activated carbons have evident advantages [24]. High SSA is generally desirable, because this parameter is related to the quantity of sites available for electrosorption, affecting the ion removal capacity. However, for these sites to be accessible, the pore size must be larger than that of the solvated ion [25]. Microporous carbons (1.0-2.0 nm) have been reported as being most suitable for electrosorption [26,27], although the presence of mesopores is also desirable, since they can act as wide avenues that facilitate the diffusion of ions to the micropores, improving the kinetics of the process [28–30]. On the other hand, while the electrosorption capacity depends on the EDL capacity, the available surface area, and the electrical potential, the electrosorption rate depends on the charge transfer rate and the ohmic drop in the solution and in the porous matrix of the electrode. Therefore, in addition to high SSA, high electronic conductivity is also desirable for a satisfactory CDI electrode.

Based on these principles, the electrode material selected in this work was carbon felt. This material differs from particulate electrodes in terms of its higher electrical conductivity, resulting from the continuity of the solid phase, which eliminates the need for binders (such as PVDF or PTFE) and conductive additives (such as carbon black). The inclusion of such materials can significantly reduce the SSA [16], while also making electrode preparation more laborious and costly. However, commercial carbon felts often have very low SSA [29]. After a search for commercially available activated carbon felts with the desired characteristics, the ACN-211-20 carbon felt, manufactured and supplied by Kynol®, was chosen for use in this work. This felt is composed of smooth and tangled fibers with average diameter of approximately 10 μm (Fig. 3a). The textural properties of the activated carbon felt were assessed by the N_2 adsorption/desorption method, employing an ASAP 2010 instrument (Micromeritics). Prior to the measurements, the samples were first degassed at 90 ºC for 18 h and then at 200 ºC for 6 h. The specific

surface area was calculated using the Brunauer-Emmett-Teller equation (SSA_{BET}), considering relative pressures (P/P_0) between 0.05 and 0.20 (the linear region of the isotherm). The total pore volume (V_T) was calculated using the 2D-NLDFT heterogeneous surface model and SAIEUS software. The micropore (V_{mic}) and mesopore (V_{mes}) volumes were determined from the volume of N_2 adsorbed by pores ≤ 2 nm and by the difference between V_T and V_{mic}, respectively. The N_2 isotherms (Fig. 3b) revealed that the material was predominantly microporous, with high specific surface area.

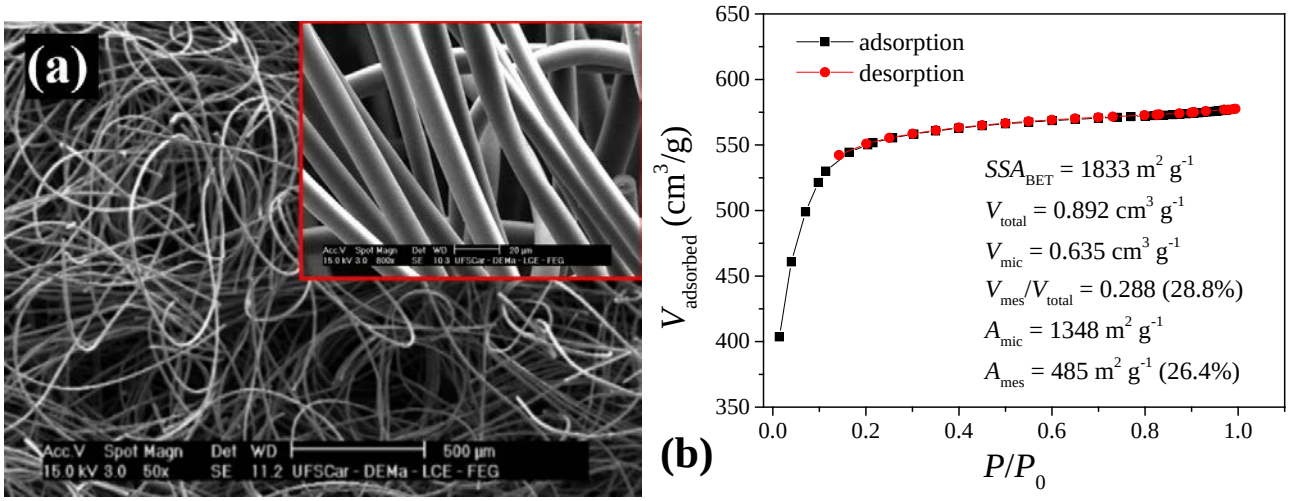

Fig. 3. (a) SEM images of the activated carbon felt electrode, at different magnifications. (b) N_2 adsorption/desorption isotherms for the activated carbon felt.

After modifying the electrodes, as indicated in Table S1, contact angle measurements were performed to assess their wettability properties. For this, a water droplet was deposited on the surface of the material and its absorption was observed using a high-precision camera. The high contact angles of the carbon felt with water (Fig. S5) indicated low wettability, with no significant differences among the functionalized samples. To improve this parameter, an additional step was performed, consisting of treatment of the CF with oxygen plasma, before reacting it with HNO_3. The modification using HNO_3 for 24 h at 60 °C was selected in these tests. For the plasma-treated samples, it was found that the water droplets were completely absorbed, making it impossible to measure a contact angle. This indicated that the carbon surface became more hydrophilic after the plasma treatment.

During the electrochemical characterizations using cyclic voltammetry, lack of reproducibility was observed, due to compression of the carbon felt in the cell (Fig. S3), which altered the electrochemical response. Hence, to obtain reliable electrochemical parameters for the evaluation of porous electrodes, such as carbon felt, it is essential that the measurements should be conducted under the same compression condition. Therefore, in the present work, a prior study of electrode compression was performed, applying different forces to the CF and obtaining R_{CT} from the EIS Nyquist plots (Fig S2.1). The results (Section S2, Supplementary Material) showed that the application of low, medium, and high compression forces led to significant differences in the electrochemical responses, as shown by the EIS spectra, so the minimum compression force required to ensure reliable measurements (Fig. S2.2) was applied for all the electrode characterizations, enabling satisfactory comparisons of the pristine and modified CFs.

3.2. Electrochemical characterizations

Cyclic voltammetry with different scan rates was employed to understand the capacitive and resistive behaviors of the samples. Firstly, to define the capacitive potential window that avoided Faradaic reactions, experiments were conducted with progressive increase of the potential from 0.0 V *vs.* Ag/AgCl (open circuit potential) to 0.5 V *vs.* Ag/AgCl. For all the electrodes, at slow scan rates (1 and 5 mV s^{-1}), the voltammograms recorded for different treatments and scan rates (Fig. S6) showed the typical quasi-rectangular shape characteristic of double-layer capacitors. However, the samples submitted to the treatments using nitric acid at 60 ºC, with and without plasma application (PCNA and CNA), were more

resistive, as indicated by the higher slopes in the voltammograms and subsequently confirmed by the EIS spectra (Fig. S7). Analogous responses were observed for the samples modified at high temperature, as shown by the shapes of the voltammograms. The capacitances calculated using Eq. 1 are shown in Fig. 4, as a function of the scan rate, with higher capacitance values obtained at 1.0 mV s^{-1} for all the modified electrodes. However, for $\nu \geq 5$ mV s^{-1}, two electrode groups were clearly evident. One group comprised the electrodes obtained using mild conditions (CNA25-12, CNA25-24, and DNA25-24), which showed no significant differences in capacitance, compared to the pristine electrode. The second group of electrodes, obtained using harsh treatments, showed a sharp capacitance decrease at faster scan rates, indicating a slow charging process and greater resistance to penetration of the ions in the carbon structure [31].

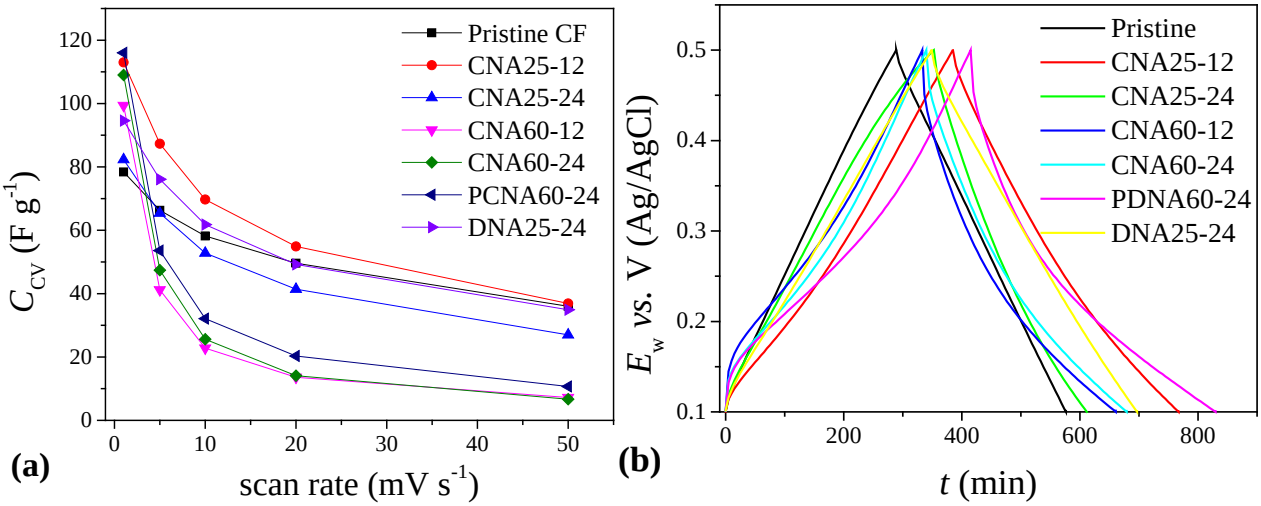

Fig. 4. (a) C_{CV} as a function of scan rate for the pristine CF and nitric acid-modified samples. (b) GCD plots for the pristine and nitric acid-modified CFs. Cutoff potentials: 0.1 V and 0.5 V *vs.* Ag/AgCl; current: 0.1 A g^{-1}.

A similar trend among the modified electrodes was observed using GCD. In Fig. 4b, the symmetry between the charge and discharge slopes represents the charge efficiency of the process, while the vertical distance between the higher potential point and the subsequent point represents the ohmic drop (IR_{drop}), which is the loss of potential due to the ohmic resistance of the material. Table S2 summarizes the values of capacitance, charge efficiency, and energy efficiency, revealing that the CNA25-12 sample combined the best conditions for these parameters. The IR_{drop} values for most of the electrodes were in the range 10-50 mV, with low values for the contact resistance between the electrode and the current collector, the solution resistance, the electrode resistivity, and the diffusion resistance [32], although the values increased for the samples submitted to harsh treatments, with highest IR_{drop} for the PCNA60-24 material.

The EIS spectra (Fig. S7) clearly showed the effect of modification using nitric acid and high temperature on the resistive behavior of the samples. Increase of the semi-circle related to R_{CT} was indicative of less efficient processes, with slower kinetics, which negatively impacted migration of the ions and, consequently, their retention in the pores of the material [33]. The samples modified at 25 °C presented less resistive behavior at medium and low frequencies, corresponding to the diffusive layer and CDI operation frequency, respectively [34]. In addition, the presence of a second semicircle in the Nyquist plots for most of the materials, except the pristine and dilute nitric acid-treated samples, indicated that the arrival of the ions at the pores of the material was hindered, imposing kinetic constraints.

Despite the different absolute values of capacitance change, according to the calculation method, most of the electrodes showed the same capacitance trend (Table S2), which indicated that it was not necessary to use longer times and high temperatures for modification of the electrode properties. In addition, although the treatment with plasma led to high capacitance using the CV technique at 1 mV s^{-1}, C_{CV} decreased exponentially at higher ν. It could be concluded from the results shown in Figs. 4 and S7 that from an engineering point of view, the use of dilute nitric acid, at room temperature, would be

sufficient to modify the electrode surface, avoiding overoxidation and reducing costs. Furthermore, the use of less nitric acid would be beneficial from an environmental perspective. Therefore, based on the electrochemical findings, the DNA25-24 electrode was selected to be modified with ethylenediamine.

Further evaluation of the electrodes modified with DNA and EDA employed different asymmetric configurations to determine the best cell setup. The pristine CF was used as the counter electrodes, while the EDA-modified electrodes obtained using different temperatures and exposure times were used as positive electrodes. The choice of these configurations was based on another important property of carbon materials used for CDI, namely the surface charge resulting from the presence of different functional groups on the surface. In the present work, the aims of the chemical treatments of the carbon were to introduce oxygen surface groups (such as carboxylic, phenolic, carbonyl, quinone, anhydride, and lactone groups), using nitric acid, and positive nitrogen functional groups, using treatment with EDA [35]. The presence of these charged surface groups acted to shift the potential of zero charge (E_{pzc}) of the electrodes, in addition to altering their hydrophilicity [18,36]. The E_{pzc} determines the degree of co-ion repulsion and the stability window of the electrode, with effects on *SAC* and electrode lifetime [16]. A schematic illustration of co-ion repulsion is shown in Fig. S8. The negative charges introduced on the carbon surface during treatment with nitric acid shifted E_{pzc} to more positive values, making the material suitable for use as a cathode (negative electrode). On the other hand, the treatment with EDA introduced nitrogen positive charges, shifting E_{pzc} to negative values and making the electrode suitable for use as an anode (positive electrode). Hence, the CNA- and DNA-modified materials were suitable for use as negative electrodes, in an asymmetric configuration, with the EDA-modified materials as positive electrodes (E_{pzc} asymmetry), employing a configuration similar to that shown in Fig. S8a, with the aim of maximizing the ion removal capacity by minimizing co-ion repulsion [37].

Fig. 5 shows the cyclic voltammograms obtained using the pristine CF and EDA-modified electrodes. Fig. S6 shows the cyclic voltammograms recorded using the CF treated with HNO_3 (to introduce SOGs) as a negative electrode. The rectangular shapes of the curves indicated pseudocapacitive behavior, while symmetry between the ascending and descending curves evidenced a stable material and reversibility of the system [38]. It should be noted that the voltammetric behavior depended on the treatment applied and, consequently, the asymmetry. However, the absolute capacitance also depended on the mass of the working electrode. The calculated C_{CV} values (Table 2) did not clearly evidence that the introduction of E_{pzc} asymmetry was an effective way to improve ion storage in the electrode. Although the surface charge modifications were effective in preventing co-ion repulsion, there was no evident relation between the electrode modification conditions (time and temperature) and capacitance. It should also be noted that the same trend observed for C_{CV} using different asymmetric configurations was observed for C_{GCD} and C_{EIS}, despite the differences in the absolute capacitance values (Figs. S9-S10 and Tables S2-S3), confirming the effectiveness of asymmetry in improving ion storage by the modified carbon felts.

Considering the best capacitance (97.5 F g^{-1}) achieved using the pristine CF|EDA105-24 asymmetric configuration, the capacitance was ~20% higher than observed using the symmetric pristine CF configuration. Given the expenditure of time, energy, and reagents in the process used to produce EDA105-12, its use would not be of interest, due to cost and environmental concerns. On the other hand, using mild conditions, as in the case of the pristine CF|EDA105-12 asymmetry, the capacitance enhancement was only 17%, which would not justify the laborious and costly process for surface modification of the carbon felt using EDA. On the other hand, using CNA25-12 as a negative electrode enhanced the capacitance by 44.3%, indicating that a simple treatment using nitric acid was able to significantly improve the deionization process by preventing energy losses associated with co-ion repulsion (Fig. S8b). It should also be noted that the plasma treatment had only a modest effect on the capacitance, so the additional costs associated with this pretreatment would not be justified.

Finally, the activated carbon felt *per se* could be considered a very attractive material for use in CDI, due to its textural properties (Fig. 3) and the substantial capacitance observed even using the symmetric configuration. To further investigate this approach, the E_{pzc} of the pristine CF was measured by EIS and compared to the resting potential, E_0. As shown in Fig. 5b, the E_{pzc} value was quite close to E_0, indicating that the pristine carbon had a neutral surface that did not significantly contribute to co-ion repulsion. Consequently, this deleterious effect was only marginal and the pristine CF could be

satisfactorily used as counter and working electrodes in a symmetric configuration, without significant loss of efficiency. Given these results, the pristine CF without surface modification was selected for use in the CDI investigation using the radial-flow cell.

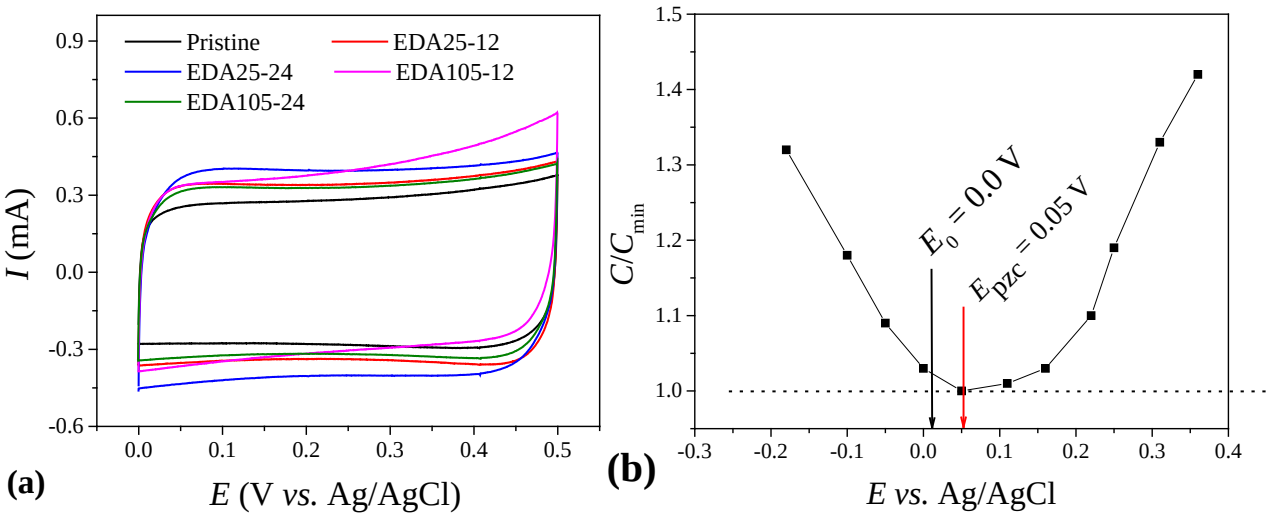

Fig. 5. (a) Cyclic voltammograms for the pristine and modified CF electrodes. (b) Normalized capacitance from EIS, according to electrode potential, for the pristine CF electrode. Experimental conditions: 1000 mg L^{-1} K_2SO_4, 10 mHz, 30 mV amplitude, and 50 mV step potential.

Table 2. C_{CV} values for different working electrodes (positive electrodes), calculated for a scan rate of 1 mV s^{-1}. The counter electrode was pristine CF.

Working electrode	C_{CV} (F g^{-1})	Working electrode	C_{CV} (F g^{-1})
Pristine CF	78.4	CNA25-12	113
EDA25-12	84.5	CNA25-24	82.3
EDA25-24	95.2	DNA25-24 h	94.6
EDA105-12	92.1	CNA60-12	99.4
EDA105-24	97.5	CNA60-24	109
		PDNA60-24	116

3.3. CDI performance

To validate the performance of the PFC employing carbon felts as both cathode and anode in a symmetric configuration, CDI experiments were performed according to the experimental sequence shown in Table 1. Experiments 1-8 investigated the effects of the variables *j*, *v*, and $\dot{V}$, while experiments 9 and 10 evaluated performances in the removal of calcium ions (Ca^{2+}), which are present at high concentrations in hard water, and the combined removal of magnesium (Mg^{2+}) and calcium, respectively. Experiment 11 employed the automated water collection system. Fig. 6 shows typical concentration profiles obtained using the galvanostatic single-pass condition, where it is possible to observe the concentration decrease during the electrosorption step and increase of the concentration during the regeneration step, starting when the cutoff voltage was reached. The long duration of the electrosorption step demonstrated the high capacity of the carbon felt to adsorb ions. Each experiment was performed with a minimum of 10 cycles and in all cases the steady state was reached after the third cycle, as shown in Fig. S11.

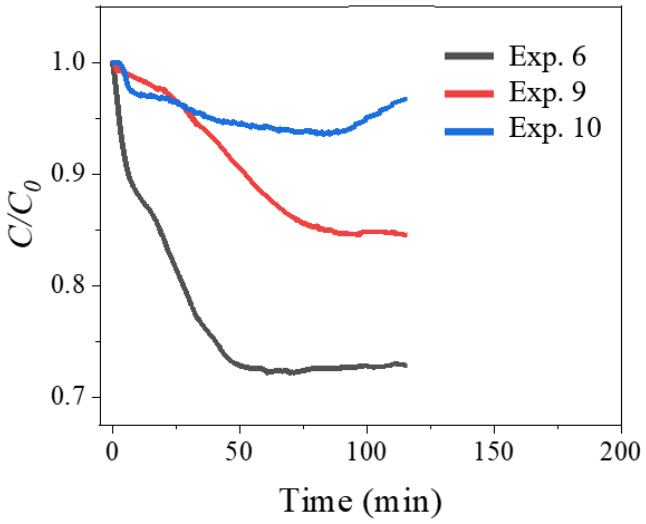

Fig. 6. Concentration profiles for galvanostatic single-pass electrosorption/desorption in experiment 6 (Mg^{2+}, j = 1.25 A m^{-2}, $\dot{\boldsymbol{V}}$ = 22 mL min^{-1}, EC), experiment 9 (Ca^{2+}, j = 1.25 A m^{-2}, $\dot{\boldsymbol{V}}$ = 22 mL min^{-1}, EC), and experiment 10 (Mg^{2+} + Ca^{2+}, j = 1.25 A m^{-2}, $\dot{\boldsymbol{V}}$ = 22 mL min^{-1}, EC).

Considering the cycles recorded under steady-state conditions, the *SAC* values were calculated using Eqs. 6-8. The results (Fig. 7a) showed that applying 1.25 A m^{-2} led to superior performance in all the experiments, especially under EC conditions. The higher *SAC* for low current densities could be attributed to improved EDL formation, according to the Gouy-Chapman-Stern (GCS) model. Although it was originally proposed for flat interfaces, the GCS model can be adopted as a local approximation to explain the relationship between the surface charge density (σ) and the surface potential (ψ), described by Eq. 10, where ε and ε_0 are the relative and vacuum permittivity, respectively, R is the gas constant, T is the absolute temperature, C_b is the bulk concentration, and z is the valence of the ions. At lower current densities, ψ increases more gradually, keeping the system under the near-linear hyperbolic sine function, resulting in more stable EDL formation and reducing co-ion repulsion effects, consequently enhancing the adsorption [39].

$$\sigma = \sqrt{8\varepsilon\varepsilon_0 RTC_b} \cdot sinh\left(\frac{zF\psi}{2RT}\right) \quad (10)$$

The flow rate also had a strong influence on CDI performance using the proposed radial-flow cell. According to the Nernst diffusion layer model, presented in Eq. 11 (where N_A is the ion flux and A_s is the surface area), a higher flow rate results in a thinner diffusion boundary layer (δ) near the electrode surface, enhancing the external mass transfer rate and facilitating the transport of ions from the bulk solution to the mouth of the pores, as shown in Fig. 1a. In the CE configuration, increasing the flow rate from 11 to 22 mL min^{-1} led to an increase of *SAC* at 1.875 A m^{-2}, but the opposite trend was observed for the EC flow pattern (Fig. 7b-c), suggesting a combined influence of the mass transfer phenomena and residence time.

Under EC flow and higher j, *SAC* performance appeared to be mainly influenced by the residence time, since at lower $\dot{\boldsymbol{V}}$ the ions remained for a longer time in contact with the porous electrode, for electrosorption to occur. On the other hand, a longer residence time at a high flow rate could limit adsorption, despite enhanced mass transport. In contrast, at lower j, external mass transfer became more critical, since the slower charging process benefited from the improved mass transfer to the electrode surface at higher flow rates, improving *SAC* performance.

$$\boldsymbol{N_A = k_m A_s (C_i - C_b)} \quad (11)$$

$$\boldsymbol{k_m = \frac{D_{iff}}{\delta}} \quad (12)$$

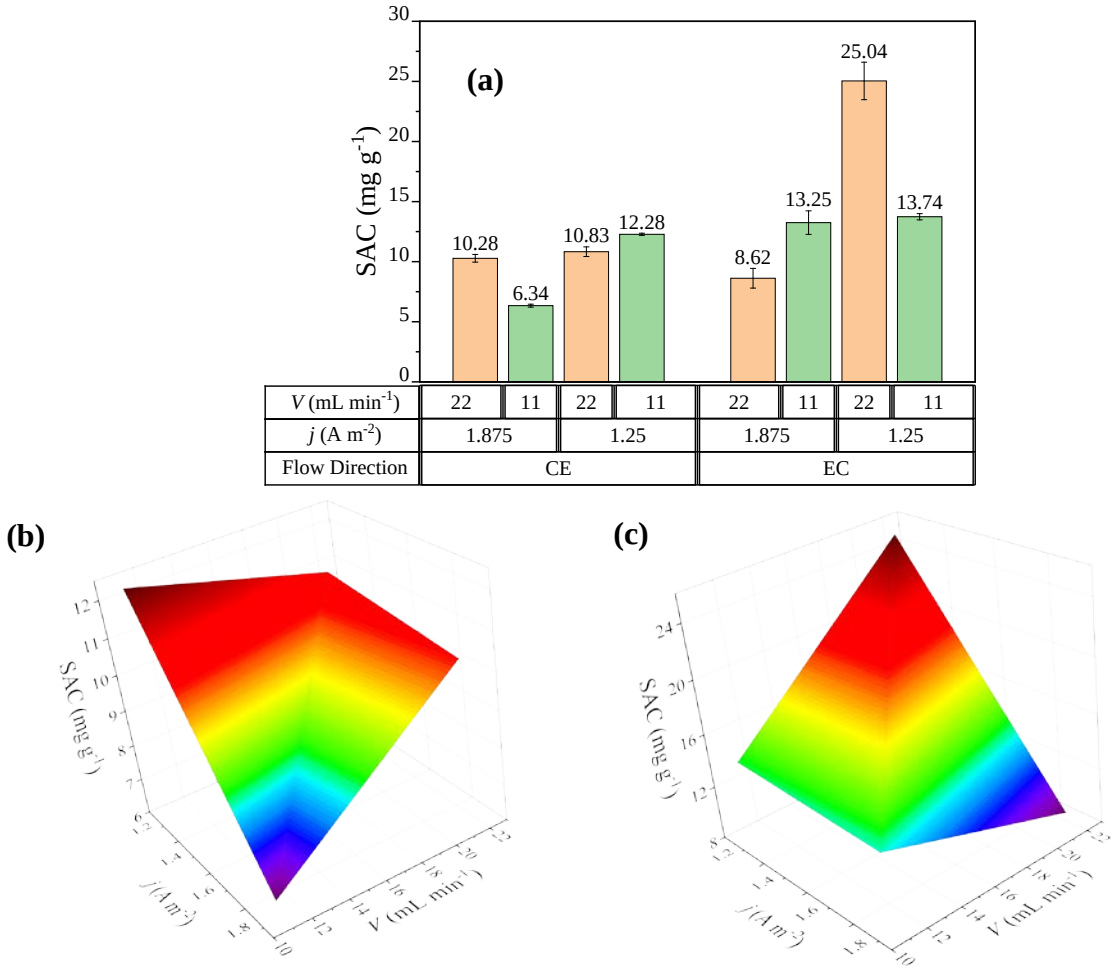

Fig. 7. (a) *SAC* as a function of j, $\dot{V}$, and flow direction. *SAC* as a function of j and $\dot{V}$ for (b) the CE and (c) the EC flow directions.

From a process engineering standpoint, it was essential to evaluate the energetic performance of the CDI system. To this end, calculations of charge efficiency and specific energy consumption were performed to assess the influence of operational parameters. As shown in Fig. 8, the flow direction from the extremities towards the center of the electrode consistently gave superior performance, enhancing both energy efficiency and ion removal. This configuration resulted in higher charge efficiency and lower energy consumption, which are critical attributes of systems designed for continuous operation and multiple regeneration cycles. Fig. S12 shows response surface plots for Q_E, evidencing the nonlinear dependence on both j and $\dot{V}$ for the two different flow patterns. Highest Q_E (100%) was achieved using the EC flow, while the maximum Q_E for CE flow was 57.4%, highlighting that the flow from the edges to the center led to superior electrochemical utilization of the applied charge. For the EC flow, ions were introduced from the extremities, leading to a more uniform and converging ionic flux towards the center. This symmetrical ion access reduced concentration polarization and favored more symmetrical EDL formation, promoting efficient ion adsorption. On the other hand, the CE configuration caused the ionic flux to diverge, which could lead to non-uniform ion penetration and localized saturation near the central region, creating a depletion zone, with suboptimal utilization of the porous electrode structure.

Energy consumption analysis confirmed that the system operated more efficiently and stably when the flow direction was from the extremities towards the center of the electrode. This can be clearly seen in Fig. 8b. Maintaining constant $\dot{V}$ and j, while varying the flow direction, the specific energy consumption (η) remained consistently lower in all the experiments using the EC flow configuration. Notably, experiment 6 not only presented the highest salt adsorption capacity, but was also the most energy-efficient condition, among all the scenarios tested.

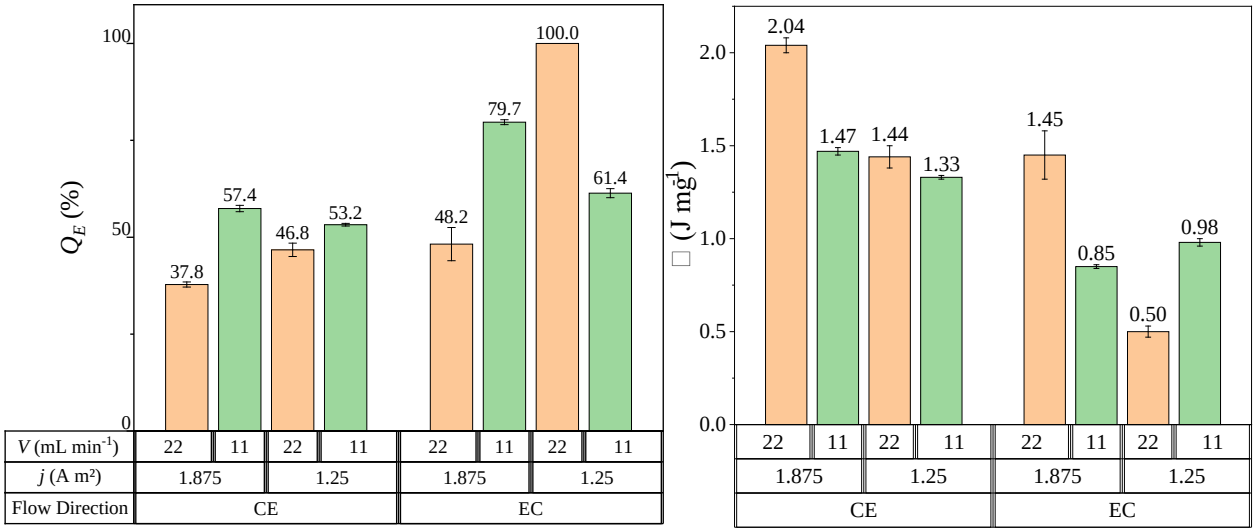

Fig. 8. (a) Q_E and (b) η as a function of j, $\dot{V}$, and flow direction.

The most effective condition was that of experiment 6, which combined a flow rate of 22 mL min^{-1}, a current density of 1.25 A m^{-2}, and a flow direction from the extremities toward the center of the electrode. This configuration enhanced ion mobility across the electrodes and facilitated the transport of ions into the porous structure. Additionally, the relatively low current density favored satisfactory EDL formation, resulting in improved system performance. This condition was evaluated in triplicate, with consistent results across the three experiments. Therefore, it was selected for use in the subsequent tests, including investigations of the removal of different ionic species, the influence of higher concentrations, and implementation of the automated water collection control system.

To understand the influence of Ca^{2+} ions and their interaction with Mg^{2+} on the performance of the percolation flow cell, experiments 9 and 10 were conducted using 500 ppm $Ca(NO_3)_2$ and a mixture of 500 ppm $Ca(NO_3)_2$ and 500 ppm $Mg(NO_3)_2$, respectively, under the previously optimized conditions. As shown in Fig. 6, the presence of magnesium ions affected the electrosorption dynamics, altering the behavior of the system, compared to the electrolyte with calcium alone. According to the literature, divalent ions tend to present stronger electrosorption than monovalent ions, due to their higher charge density [26]. However, among divalent ions, specific physicochemical properties, such as ionic radius and hydration energy, have important effects. Mg^{2+} has a tightly bound hydration shell, which can stabilize its transport, leading to easier formation of the EDL. On the other hand, Ca^{2+}, despite having the same valency, has a larger ionic radius and lower hydration enthalpy, which could lead to less compact EDL formation and lower electrosorption efficiency [40]. The results of experiments 9 and 10, in terms of performance variables, are compiled in Table 3. Relative proximity between these experiments, in terms of *SAC*, Q_E, and η, indicated that the effects related to the presence of Ca^{2+} during the adsorption process were significantly more important than the interaction between Ca^{2+} and Mg^{2+}.

Table 3. Comparison of experiments 6, 9, and 10, in terms of *SAC*, Q_E, and η.

Exp.	i (A m^{-2})	$\dot{V}$ (mL min^{-1})	Flow direction	*SAC* (mg g^{-1})	Q_E (%)	η (J mg^{-1})
6	1.25	22	EC	25.0 ± 1.6	100	0.5
9				11.2 ± 0.1	53.8 ± 0.7	1.0
10				9.5 ± 0.8	51 ± 4	1.2

3.4. Automated water collector system performance

Evaluation was made of the performance of the proposed automated water collection system, under the optimized conditions. From an engineering and practical application perspective, two main objectives were considered: (i) ensuring that only softened water was collected as the final product, and (ii) implementing a cost-effective and reliable control strategy using readily available components.

To fulfill these requirements, the ESP-32 microcontroller (Fig. S1.1b) was selected, due to its low cost, extensive documentation, and built-in wireless communication protocols, which enable potential integration with remote monitoring systems. The electronic control system, shown in Fig. S1.1a, incorporated a low-cost commercial conductivity sensor (Fig. S1.1c), installed at the system outlet, which continuously monitored water conductivity. The sensor output was processed by the microcontroller, which applied a predefined threshold to classify the stream. When the conductivity exceeded this setpoint, the ESP-32 triggered a BC548 NPN transistor, which in turn activated a relay circuit connected to a three-way solenoid valve that controlled the collection flow. To prevent circuit damage, two diodes were added, one in a flyback freewheeling configuration across the relay coil, to suppress inductive voltage spikes when switching the relay, and the second to protect the output pin of the microcontroller against reverse current. Fig. S1.2 compares the low-cost conductivity sensor with a laboratory-grade sensor. Although an offset can be seen between the curves, due to hysteresis for the low-cost sensor (Fig. S1.3), visible as a vertical shift along the y-axis, the low-cost sensor effectively tracked the concentration profile of the reference instrument. This confirmed its suitability as a viable and affordable option for commercial applications.

Before experiment 11, the sensor was calibrated by acquiring data for one cycle of electrosorption. The response curve was fitted using an equation based on conversion of the output voltage to the concentration profile. For experiment 11, a 6 L solution of 500 mg L^{-1} $Mg(NO_3)_2$ was prepared as the electrolyte, with the use of a larger volume allowing simulation of a full electrosorption cycle. A single container was used as the feed reservoir, while two containers at the cell outlet separately collected the product and the waste. The concentration threshold was defined as 300 mg L^{-1} and the two conductivity meters (laboratory-grade and low-cost) were installed together to compare the curve profiles. The softened water collected in the product reservoir had a final concentration of 260 mg L^{-1}, demonstrating the effectiveness of the control system in satisfactorily managing the outlet stream of the cell. The results confirmed the ability of the system to convert very hard water into hard water, achieving a quality level that complied with Brazilian drinking water standards. Therefore, the implemented control strategy successfully ensured that the treated water complied with acceptable hardness limits for public water supply.

After the electrochemical system reached steady-state conditions, the control system was activated and the performance of the PFC was evaluated using the water recovery (*WR*) metric, defined as the ratio between the product and the total electrolyte volume (Eq. 9). For a total flow volume of 2206 mL in one cycle, 713 mL was recovered as product stream, resulting in *WR* of 32.3 %. This low value indicated that further improvements could be achieved by reducing the desorption time, during which the greatest part of the output stream was discarded. Strategies such as applying different current densities for the adsorption and desorption phases, or automatic flow rate control, could accelerate ion removal from the cell, consequently improving *WR*.

4. Conclusions

This aim of this work was to investigate the use of capacitive deionization (CDI) as an electrochemical process to produce deionized water. For this purpose, evaluation was made of the effects of different surface modification strategies on electrode properties, focusing on the way that surface functional groups could influence capacitive behavior. These modifications were also assessed considering their economic and environmental impacts. The results indicated that the chemical treatments applied to the electrode, using nitric acid and ethylenediamine, altered the surface chemistry and improved capacitive performance. The enhancement obtained using EDA was modest, compared to the use of DNA. The best-performing EDA-modified electrode showed only a 20% increase in capacitance, compared to 44.3% using the CNA25-12 electrode, as determined by cyclic voltammetry. Therefore, it could be concluded that the modest improvement achieved using EDA was insufficient to justify use of this modification in the CDI system, especially when balancing performance gains against economic and environmental costs. On the other hand, the application of a simple and low-cost treatment using nitric acid was shown to be highly effective for improving electrode performance.

The performance of the designed radial-flow cell showed a significant dependence on the electrode flow direction, which could be attributed to differences in mass transfer and electrosorption kinetics. The flow direction from the extremities toward the center of the electrode enhanced the formation of the electrical double layer (EDL), while mitigating co-ion repulsion effects. This configuration provided a more uniform ionic flux convergence, improving charge efficiency and ion transport within the porous electrode structure. Furthermore, the proposed cell design offers advantages in scalability, both vertically and horizontally, making it a promising solution not only for residential water treatment, but also for industrial water softening applications.

Process variables were also shown to have a significant influence on the capacitive deionization, with the selection of appropriate flow rate and current density being essential for simultaneously maximizing the salt adsorption capacity and minimizing energy consumption. The optimal operational conditions were a flow rate of 22 mL min^{-1} and a current density of 1.25 A m^{-2}. Under these conditions, combined with the EC flow direction, the system achieved a SAC of 25.04 mg g^{-1} and a specific energy consumption of 0.50 J mg^{-1}. These results demonstrated a satisfactory balance between performance and energy efficiency, highlighting the potential of this system for use in practical domestic and commercial water treatment applications.

The automated water collection system provided valuable insights into the practical operation of the CDI process. Although the water recovery achieved under the tested conditions was relatively low, limiting its immediate competitiveness for large-scale applications, it is expected that system scale-up would significantly enhance this parameter. The combination of precise control achieved using the three-way solenoid valve, a low-cost conductivity sensor, and an ESP-32 microcontroller provides a system with potential as a cost-effective, reliable, and innovative solution for water softening. The ability to develop a fully integrated CDI unit incorporating automated product recovery, with potential for further optimization, paves the way towards feasible commercial applications.

Acknowledgments

The authors are grateful to the São Paulo State Research Foundation (FAPESP, grants 2020/12706-9 and 2023/06600-1) for financial support. Bruno G. M. Alves is indebted to FAPESP for a fellowship (grants 2023/08483-2 and 2023/15868-8).

References

[1] G.L. Muniz, F.V. Duarte, M. Rakocevic, Assessment and optimization of carbonated hard water softening with Moringa oleifera seeds, Desalination Water Treat 173 (2020) 156–165. https://doi.org/10.5004/dwt.2020.24745.

[2] S.J. Seo, H. Jeon, J.K. Lee, G.Y. Kim, D. Park, H. Nojima, J. Lee, S.H. Moon, Investigation on removal of hardness ions by capacitive deionization (CDI) for water softening applications, Water Res 44 (2010) 2267–2275. https://doi.org/10.1016/j.watres.2009.10.020.

[3] M.A. Anderson, A.L. Cudero, J. Palma, Capacitive deionization as an electrochemical means of saving energy and delivering clean water. Comparison to present desalination practices: Will it compete?, Electrochim Acta 55 (2010) 3845–3856. https://doi.org/10.1016/j.electacta.2010.02.012.

[4] M.E. Suss, S. Porada, X. Sun, P.M. Biesheuvel, J. Yoon, V. Presser, Water desalination via capacitive deionization: What is it and what can we expect from it?, Energy Environ Sci 8 (2015) 2296–2319. https://doi.org/10.1039/c5ee00519a.

[5] J.C. Farmer, D.V. Fix, G.V. Mack, R.W. Pekala, J.F. Poco, Capacitive Deionization of NaCl and NaNO3 Solutions with Carbon Aerogel Electrodes, J Electrochem Soc 143 (1996) 159–169. https://doi.org/10.1149/1.1836402.

[6] W. Xing, J. Liang, W. Tang, D. He, M. Yan, X. Wang, Y. Luo, N. Tang, M. Huang, Versatile applications of capacitive deionization (CDI)-based technologies, Desalination 482 (2020) 114390. https://doi.org/10.1016/j.desal.2020.114390.

[7] E. García-Quismondo, C. Santos, J. Lado, J. Palma, M.A. Anderson, Optimizing the energy efficiency of capacitive deionization reactors working under real-world conditions, Environ Sci Technol 47 (2013) 11866–11872. https://doi.org/10.1021/es4021603.

[8] C. Tan, C. He, J. Fletcher, T.D. Waite, Energy recovery in pilot scale membrane CDI treatment of brackish waters, Water Res 168 (2020) 115146. https://doi.org/10.1016/j.watres.2019.115146.

[9] P.T. Juchen, L.A.M. Ruotolo, Roles of mass transfer and cell architecture in electrochemical desalination performance using polyglycerol activated carbon electrodes, Chem Eng J 452 (2023) 139226. https://doi.org/10.1016/j.cej.2022.139226.

[10] O. Sufiani, J. Elisadiki, R.L. Machunda, Y.A.C. Jande, Modification strategies to enhance electrosorption performance of activated carbon electrodes for capacitive deionization applications, J Electroanal Chem 848 (2019) 113328. https://doi.org/10.1016/j.jelechem.2019.113328.

[11] C.-T. Hsieh, H. Teng, Influence of oxygen treatment on electric double-layer capacitance of activated carbon fabrics, Carbon 40 (2002) 667–674. https://doi.org/10.1016/S0008-6223(01)00182-8

[12] A. Pedico, S. Bocchini, E. Tresso, A. Lamberti, Enhanced Capacitive Deionization Exploiting Novel Functionalized Graphene Oxide Electrodes, Adv Mater Technol 7 (2022) 2101513. https://doi.org/10.1002/admt.202101513.

[13] W. Tang, J. Liang, D. He, J. Gong, L. Tang, Z. Liu, D. Wang, G. Zeng, Various cell architectures of capacitive deionization: Recent advances and future trends, Water Res 150 (2019) 225–251. https://doi.org/10.1016/j.watres.2018.11.064.

[14] S.D. Datar, K. Mohanapriya, D.J. Ahirrao, N. Jha, Comparative study of electrosorption performance of solar reduced graphene oxide in flow-between and flow-through capacitive deionization architectures, Sep Purif Technol 257 (2021) 117972. https://doi.org/10.1016/j.seppur.2020.117972.

[15] E.M. Remillard, A.N. Shocron, J. Rahill, M.E. Suss, C.D. Vecitis, A direct comparison of flow-by and flow-through capacitive deionization, Desalination 444 (2018) 169–177. https://doi.org/10.1016/j.desal.2018.01.018.

[16] K.M. Barcelos, K.S.G.C. Oliveira, L.A.M. Ruotolo, Insights on the role of interparticle porosity and electrode thickness on capacitive deionization performance for desalination, Desalination 492 (2020) 114594. https://doi.org/10.1016/j.desal.2020.114594.

[17] P.T. Juchen, K.M. Barcelos, K.S.G.C. Oliveira, L.A.M. Ruotolo, Using crude residual glycerol as precursor of sustainable activated carbon electrodes for capacitive deionization desalination, Chem Eng J 429 (2022) 132209. https://doi.org/10.1016/j.cej.2021.132209.

[18] M. Vujković, N. Gavrilov, I. Pašti, J. Krstić, J. Travas-Sejdic, G. Ćirić-Marjanović, S. Mentus, Superior capacitive and electrocatalytic properties of carbonized nanostructured polyaniline upon a low-temperature hydrothermal treatment, Carbon N Y 64 (2013) 472–486. https://doi.org/10.1016/j.carbon.2013.07.100.

[19] F. Licht, M.A. Davis, H.A. Andreas, Charge redistribution and electrode history impact galvanostatic charging/discharging and associated figures of merit, J Power Sources 446 (2020) 227354. https://doi.org/10.1016/j.jpowsour.2019.227354.

[20] R. Zhao, P.M. Biesheuvel, A. Van Der Wal, Energy consumption and constant current operation in membrane capacitive deionization, Energy Environ Sci 5 (2012) 9520–9527. https://doi.org/10.1039/c2ee21737f.

[21] C. Zhang, D. He, J. Ma, W. Tang, T.D. Waite, Comparison of faradaic reactions in flow-through and flow-by capacitive deionization (CDI) systems, Electrochim Acta 299 (2019) 727–735. https://doi.org/10.1016/j.electacta.2019.01.058.

[22] Y. Oren, Capacitive deionization (CDI) for desalination and water treatment - past, present and future (a review), Desalination 228 (2008) 10–29. https://doi.org/10.1016/j.desal.2007.08.005.

[23] M. Tauk, G. Folaranmi, M. Cretin, M. Bechelany, P. Sistat, C. Zhang, F. Zaviska, Recent advances in capacitive deionization: A comprehensive review on electrode materials, J Environ Chem Eng 11 (2023) 111368. https://doi.org/10.1016/j.jece.2023.111368.

[24] F.A. Al Marzooqi, A.A. Al Ghaferi, I. Saadat, N. Hilal, Application of Capacitive Deionisation in water desalination: A review, Desalination 342 (2014) 3–15. https://doi.org/10.1016/j.desal.2014.02.031.

[25] C.J. Gabelich, T.D. Tran, I.H. Suffet, Electrosorption of inorganic salts from aqueous solution using carbon aerogels, Environ Sci Technol 36 (2002) 3010–3019. https://doi.org/10.1021/es0112745.

[26] S. Porada, R. Zhao, A. Van Der Wal, V. Presser, P.M. Biesheuvel, Review on the science and technology of water desalination by capacitive deionization, Prog Mater Sci 58 (2013) 1388–1442. https://doi.org/10.1016/j.pmatsci.2013.03.005.

[27] C.L. Yeh, H.C. Hsi, K.C. Li, C.H. Hou, Improved performance in capacitive deionization of activated carbon electrodes with a tunable mesopore and micropore ratio, Desalination 367 (2015) 60–68. https://doi.org/10.1016/j.desal.2015.03.035.

[28] C. Tsouris, R. Mayes, J. Kiggans, K. Sharma, S. Yiacoumi, D. Depaoli, S. Dai, Mesoporous carbon for capacitive deionization of saline water, Environ Sci Technol 45 (2011) 10243–10249. https://doi.org/10.1021/es201551e.

[29] R.L. Zornitta, J.J. Lado, M.A. Anderson, L.A.M. Ruotolo, Effect of electrode properties and operational parameters on capacitive deionization using low-cost commercial carbons, Sep Purif Technol 158 (2016) 39–52. https://doi.org/10.1016/j.seppur.2015.11.043.

[30] L. Zou, L. Li, H. Song, G. Morris, Using mesoporous carbon electrodes for brackish water desalination, Water Res 42 (2008) 2340–2348. https://doi.org/10.1016/j.watres.2007.12.022.

[31] J.J. Lado, R.L. Zornitta, F.A. Calvi, M.I. Tejedor-Tejedor, M.A. Anderson, L.A.M. Ruotolo, Study of sugar cane bagasse fly ash as electrode material for capacitive deionization, J Anal Appl Pyrolysis 120 (2016) 389–398. https://doi.org/10.1016/j.jaap.2016.06.009.

[32] S. Zhao, T. Yan, H. Wang, G. Chen, L. Huang, J. Zhang, L. Shi, D. Zhang, High capacity and high rate capability of nitrogen-doped porous hollow carbon spheres for capacitive deionization, Appl Surf Sci 369 (2016) 460–469. https://doi.org/10.1016/j.apsusc.2016.02.085.

[33] A. Hauch, A. Georg, Diffusion in the electrolyte and charge-transfer reaction at the platinum electrode in dye-sensitized solar cells, Electrochim Acta 46 (2001) 3457–3466. www.elsevier.com/locate/electacta.

[34] B.A. Mei, O. Munteshari, J. Lau, B. Dunn, L. Pilon, Physical Interpretations of Nyquist Plots for EDLC Electrodes and Devices, J Phys Chem C 122 (2018) 194–206. https://doi.org/10.1021/acs.jpcc.7b10582.

[35] X. Gao, S. Porada, A. Omosebi, K.L. Liu, P.M. Biesheuvel, J. Landon, Complementary surface charge for enhanced capacitive deionization, Water Res 92 (2016) 275–282. https://doi.org/10.1016/j.watres.2016.01.048.

[36] J.J. Lado, R.L. Zornitta, F.A. Calvi, M. Martins, M.A. Anderson, F.G.E. Nogueira, L.A.M. Ruotolo, Enhanced capacitive deionization desalination provided by chemical activation of sugar cane bagasse fly ash electrodes, J Anal Appl Pyrolysis 126 (2017) 143–153. https://doi.org/10.1016/j.jaap.2017.06.014.

[37] R.L. Zornitta, K.M. Barcelos, F.G.E. Nogueira, L.A.M. Ruotolo, Understanding the mechanism of carbonization and KOH activation of polyaniline leading to enhanced electrosorption performance, Carbon N Y 156 (2020) 346–358. https://doi.org/10.1016/j.carbon.2019.09.058.

[38] Y. Uchida, E. Kätelhön, R.G. Compton, Cyclic voltammetry with non-triangular waveforms: Electrochemically irreversible and quasi-reversible systems, J Electroanal Chem 810 (2018) 135–144. https://doi.org/10.1016/j.jelechem.2017.12.053.

[39] A. Allagui, H. Benaoum, O. Olendski, On the Gouy–Chapman–Stern model of the electrical double-layer structure with a generalized Boltzmann factor, Physica A: Stat Mech Appl 582 (2021) 126252. https://doi.org/10.1016/j.physa.2021.126252.

[40] Y. Marcus, Thermodynamics of solvation of ions. Part 5. - Gibbs free energy of hydration at 298.15 K, J Chem Soc Faraday Trans 87 (1991) 2995–2999. https://doi.org/10.1039/FT9918702995.